

Aerodynamics of Low Reynolds Number Axial Compressor Sections

Andrea Maffioli*

Cesare A. Hall†

Sam Melvin‡

Whittle Laboratory, University of Cambridge, 1 JJ Thomson Avenue, Cambridge CB3 0DY, United Kingdom

Compact compression systems are of interest for the domestic appliance industry. The associated low Reynolds number leads to a flow regime in which the losses rise dramatically compared to large-scale compressors due to a transitional flow field with large regions of separation. We explore this uncharted design space in terms of axial compressor sections with varying thickness distribution and inlet and exit angles using a coupled free-stream/boundary layer solver. We find that the amount of turning such blades can impart is reduced compared to high- Re applications, and that this problem is increased at low flow coefficients, i.e. high inlet angles. By varying the position of the maximum thickness point along the blade chord, we discovered that moving the thickness towards the front encourages early transition over the thickness “bump” leaving the turbulent flow downstream with a mild adverse pressure gradient with a now slowly decreasing blade thickness. Hence turbulent separation on such front-thickened blades is delayed leading to lower loss and deviation. We also study the effect of pitch-to-chord ratio and observe that there is a trade-off between design efficiency and incidence range as the blade spacing is increased. A compromise value leads to a Lieblein diffusion factor $D_F = 0.45$, which is the conservative value typically used in large-scale compressor design. Finally experiments with linear cascades created from the blade designs highlight the challenge in accurately capturing the laminar separation bubble on the suction surface, and suggest a move towards high-fidelity numerical simulations for future research in low- Re compressors.

Nomenclature

c	Blade chord
d	Distance along camber line or blade suction surface
i	Incidence angle, $i = \beta_1 - \chi_1$
p	Pressure
s	Blade pitch
t	Blade thickness
x	Axial direction
y	Blade-to-blade direction
z	Blade half-thickness
$C(x)$	Class function, $C(x) = \sqrt{x}(1 - x)$
C_P	Pressure coefficient, $C_P = (p - p_1)/(p_{01} - p_1)$
D_F	Lieblein diffusion factor
M	Mach number
Re	Reynolds number, $Re = \rho W_1 c / \mu$
$S(x)$	Shape function
T	Temperature
U	Blade rotational speed

*Research Associate, Whittle Laboratory, 1 JJ Thomson Avenue, Cambridge, UK.

†Senior Lecturer, Whittle Laboratory, 1 JJ Thomson Avenue, Cambridge, UK.

‡M.Eng Student, Cambridge University Engineering Department, Trumpington Street, Cambridge, UK.

\mathbf{V}	Flow velocity in absolute frame
\mathbf{W}	Flow velocity in relative frame
Y_P	Loss coefficient
β	Flow angle
δ	Deviation angle, $\delta = \beta_2 - \chi_2$
η	Rotor efficiency, $\eta = (T_{02s} - T_{01}) / (T_{02} - T_{01})$
ϕ	Flow coefficient
ψ	Stage loading coefficient
μ	Dynamic viscosity
ρ	Density
χ	Blade metal angle
$\Delta\chi$	Blade camber, $\Delta\chi = \chi_1 - \chi_2$
<i>Subscript</i>	
0	Stagnation quantity
1	Inlet
2	Outlet
θ	Tangential
s	Isentropic
max	Corresponding to maximum thickness point
rel	Rotor relative frame
te	Trailing edge
trans	Corresponding to transition location on suction side
<i>Superscript</i>	
*	Design conditions, $i = -3^\circ$

I. Introduction

The domestic appliance industry requires small-size compression systems for their air-flow devices, which range from vacuum cleaners, to desk fans, to hand and hair dryers. Historically the design choice has been centrifugal compressors rotating at high speeds to provide the necessary pressure rise. More recently there has been a drive towards more efficient and even more compact compressors, two conditions which could be met by axial compressors. The low Reynolds number associated with these centimeter-scale devices leads to a transitional flow field on the compressor blades, a factor which is typically not taken into account for larger scale applications such as jet engines. The result is that there is an unexplored design space in terms of axial compressors operating at Reynolds numbers in the range $Re = 2 \times 10^4 - 2 \times 10^5$ (based on relative speed into the rotor and rotor chord). High rotational speeds are necessary to obtain the desired pressure rise over what is typically a single-stage compressor configuration, which leads to compressible Mach numbers. In this first design study however we will limit our investigation to incompressible Mach numbers, focusing mainly on the Reynolds number effect, and choosing a representative Reynold number $Re = 5 \times 10^4$ for most of our numerical and experimental runs.

To demonstrate the Reynolds number effect we have run solutions for a generic blade over a range of Reynolds numbers. The results in terms of stagnation pressure loss coefficient Y_P can be seen in Figure 1 and it is evident that there is a significant rise in the overall 2D loss at Reynolds numbers below about 1.5×10^5 . At higher Reynolds numbers the loss coefficient asymptotes out to a value just below $Y_P = 0.02$. To obtain the overall losses across the rotor the endwall and tip leakage losses also have to be considered. A previous study at similar Reynolds numbers, albeit using a fully turbulent flow prescription, found that in addition to the 2D profile losses, also the endwall losses significantly increase at low- Re (while in this study the tip leakage losses actually decreased) leading to a significantly increased overall 3D loss.¹ It is now clear that it a serious challenge to design efficient compression systems in this flow regime.

Let us now explore the physics of low Reynolds number aerodynamics. In the case of isolated aerofoils, the performance in terms of lift-to-drag ratio is degraded at low Reynolds numbers due to the predominant presence of laminar separation. This can be in the form of a laminar separation bubble, where the separation-induced transition to turbulence leads to the downstream re-attachment of the free shear layer and to the formation of a closed separation region. If the Reynolds number is sufficiently low or if the adverse pressure

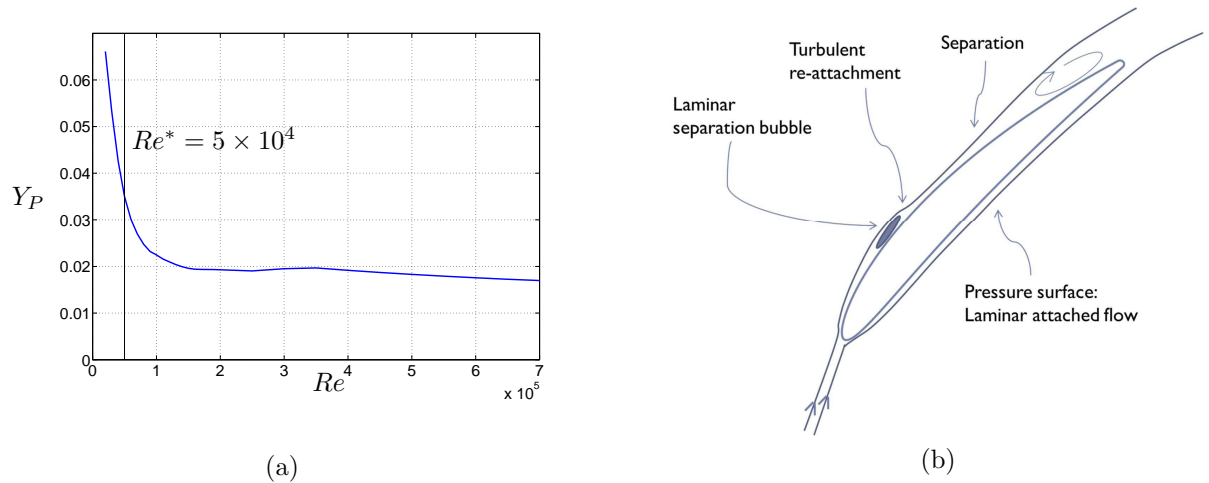


Figure 1. (a) Loss coefficient at zero incidence for varying Reynolds numbers. Blade section is a C4 blade with 25° turning, maximum thickness of 8% chord and 1.2 pitch-to-chord ratio. Vertical line showing the Reynolds number of this study Re^* . (b) Sketch of flow around a 2D blade at Re^* .

gradient is high enough, there will be no turbulent re-attachment and we are in the presence of an open laminar separation.² Similar features will be important in the case of a two-dimensional cascade of blades, although the flow guidance due to the periodic repetition of blades is expected to relieve the adverse pressure gradients on the blades compared to an isolated aerofoil, leading to smaller separation regions for the same Reynolds number and flow turning. It has been suggested previously that at “subcritical Reynolds numbers” (which could be defined as $Re < 1.5 \times 10^5$ using Figure 1 as a guidance) any factors that encourage early transition, such as the use of trip wires or high free-stream turbulence, will be beneficial.³ This is because in these two scenarios the laminar separation bubble will be reduced in extent and, in the case of an optimally sized and placed boundary layer trip, could be completely avoided, thus greatly reducing the losses. Due to the low Re encountered in low pressure turbines, laminar separation bubbles have been studied for turbine representative pressure distribution both experimentally⁴ and numerically.⁵ Relatively large separation bubbles have been found in these studies downstream of the suction peak starting at about half-chord. The case of compressor flows at low Re has not been treated extensively because of the high Re nature of jet engine and industrial compressor stages. It is expected that the different pressure distribution, in particular the very early suction peak and the presence of an adverse pressure gradient on the vast majority of compressor blades suction surfaces, will lead to a substantially different flow picture. A sketch of the flow field we computed is given for our representative Reynolds number, $Re = 50,000$, in Figure 1(b). The salient flow features over the blade section in cascade configuration are highlighted: on the suction surface the flow is initially laminar and separates after some distance — dependent on the exact flow angle and blade shape — and then promptly transitions to turbulence and reattaches closing the laminar separation bubble. In most cases the flow then presents a further (turbulent) separation downstream that does not reattach. The pressure surface, on the other hand, is largely covered by laminar attached flow, except at severely negative incidence. Hence it is expected that the suction surface, with its series of separations, determines the loss on such blade sections. We will therefore concentrate on suction side performance in our design study, with the principal aim of reducing the separation regions on this blade surface.

This paper is organized as follows: in Section II we present the numerical methods and introduce the design parameters, and in Section III results from the design investigation are presented. We start by looking at the effect of the blade inlet and exit angles, then continue by exploring the blade thickness distribution and in particular the location of the maximum thickness and the section is concluded by presenting a modified Smith Chart for a blade shape performing well at low Reynolds numbers and by considering the effect of varying the pitch-to-chord ratio. In Section IV we present flow visualisations and results from a series of tests on cascades using an early and an optimized design from the MISES exploration. We finish with a discussion on future work on low Reynolds number compressors and with some concluding remarks in Section V.

II. Methodology

Our chosen flow solver is MISES, a coupled Euler free-stream/integral boundary layer method with a transition model.⁶ This solver uses a modified e^n transition model, a variant of which has been shown to be successful in accurately capturing laminar separation induced transition over low Reynolds number airfoils.⁷ There is evidence that the solver MISES is based on correctly predicts the performance degradation as we decrease the Reynolds number⁸ although to our knowledge there are no publications using this solver at Reynolds numbers as low as the ones we are considering. Thus the experimental cascade tests presented in Section IV also serve as a test on the validity of MISES at such low Re .

The MISES solver simulates a linear cascade of blades, whose geometry is given in Figure 2(a). The incoming flow W_1 makes an angle β_1 with the x -direction and leaves the cascade at an angle β_2 . These angles with respect to the local blade metal angles (respectively χ_1 and χ_2), are the incidence i and the deviation δ . The change in blade metal angles, or blade camber, is $\Delta\chi = \chi_1 - \chi_2$. With an application to a compressor rotor in mind, we consider the blade sections to be mean-radius sections for a rotor with zero inlet swirl. Hence we take the sections to be in the rotating frame of reference, with the x -direction corresponding to the axial direction in the compressor and the y -direction corresponding to the circumferential direction. The zero inlet swirl condition means the inlet velocity in the absolute frame V_1 is in the axial direction. As a result V_1 is the x -component of W_1 , i.e. $V_1 = W_1 \cos \beta_1$ and it also follows that the assumed rotational speed is $U = W_1 \sin \beta_1$. Under these assumptions, the flow coefficient is $\phi \equiv V_x/U = V_1/U = 1/\tan \beta_1$, and our design flow coefficient taken at $i = -3^\circ$ is therefore $\phi^* = 1/\tan(\chi_1 - 3^\circ)$. The stage loading coefficient is

$$\psi \equiv \frac{\Delta h_0}{U^2} = \frac{U \Delta V_\theta}{U^2} = \frac{V_{\theta 2}}{U} = \frac{U - W_{\theta 2}}{U} = 1 - \frac{W_{\theta 2}}{U}, \quad (1)$$

where Euler's turbine equation has been used in the first step and the zero inlet swirl condition in the second step ($V_{\theta 1} = 0$). For design purposes we approximate the last expression for the stage loading as $\psi^* = 1 - \phi^* \tan \beta_2^*$ assuming the axial velocity to be constant and $\beta_2^* = \chi_2 + \delta^*$ with $\delta^* = 11^\circ$.

In most of the design study the pitch-to-chord ratio is fixed using a constant diffusion factor $D_F^* = 0.425$ at design. The Lieblein diffusion factor is defined as

$$D_F \equiv \frac{W_1 - W_2}{W_1} + \frac{s}{c} \frac{W_{\theta 1} - W_{\theta 2}}{2W_1} \quad (2)$$

where from the pitch-to-chord ratio s/c can be computed using the design estimates delineated above. In the original analysis⁹ the limiting diffusion factor above which large separations occurred was identified to be $D_F = 0.6$. In modern compressor design a more conservative value is used, typically $D_F \approx 0.45$, to ensure a reasonable stall margin.¹⁰

One of the main MISES outputs we use is the stagnation pressure loss coefficient

$$Y_P \equiv \frac{(p_{01,\text{rel}} - p_{02,\text{rel}})}{(p_{01,\text{rel}} - p_1)}, \quad (3)$$

defined in the MISES relative frame. It is a measure of the entropy creation in the blade boundary layers and in the wakes; this entropy generation arises only from the decrease in stagnation pressure p_0 across the cascade since $T_{02,\text{rel}} = T_{01,\text{rel}}$ (no work is being done on the flow in the relative frame) and so there are no stagnation temperature effects. Under our assumptions, a rotor efficiency based on the 2D flow can be defined as:

$$\eta \equiv \frac{T_{02s} - T_{01}}{T_{02} - T_{01}} = \frac{\left(\frac{p_{02}}{p_{01}}\right)^{\gamma-1/\gamma} - 1}{\frac{T_{02}}{T_{01}} - 1} \quad (4)$$

and computed using outputs from the MISES runs, on noting that all quantities involved are in the absolute frame and so a change of frame of reference has to be applied to the computation results in the relative frame.

In Figure 2(b) the pressure coefficient for a C4 blade at design incidence is compared against that of an optimised shape-class blade. Details of both thickness distributions will be given in Section III. Design parameters for both blades are given in Table 1, where values for loss coefficient, deviation and rotor efficiency

are added for comparison. The only difference between the two blade sections considered is the thickness distribution, and in particular the location of the maximum thickness point, which in the shape-class blade is brought forwards to 20% chord. The resulting pressure distribution on the shape-class blade presents an approximately constant diffusion (constant pressure gradient) on the suction surface, resulting in a “fuller” pressure distribution than the C4 blade C_P distribution. This single modification leads to a 1.5% increase in efficiency. More performance gains can be found by modifying the remaining three design parameters: flow coefficient ϕ^* , stage loading coefficient ψ^* and pitch-to-chord ratio s/c (while the blade angles χ_1 and χ_2 are design inputs are not independent from ϕ^* and ψ^* as seen above). In what follows, we will explore the design space in terms of these design parameters, starting from the baseline C4 thickness distribution laid onto a circular camber line.

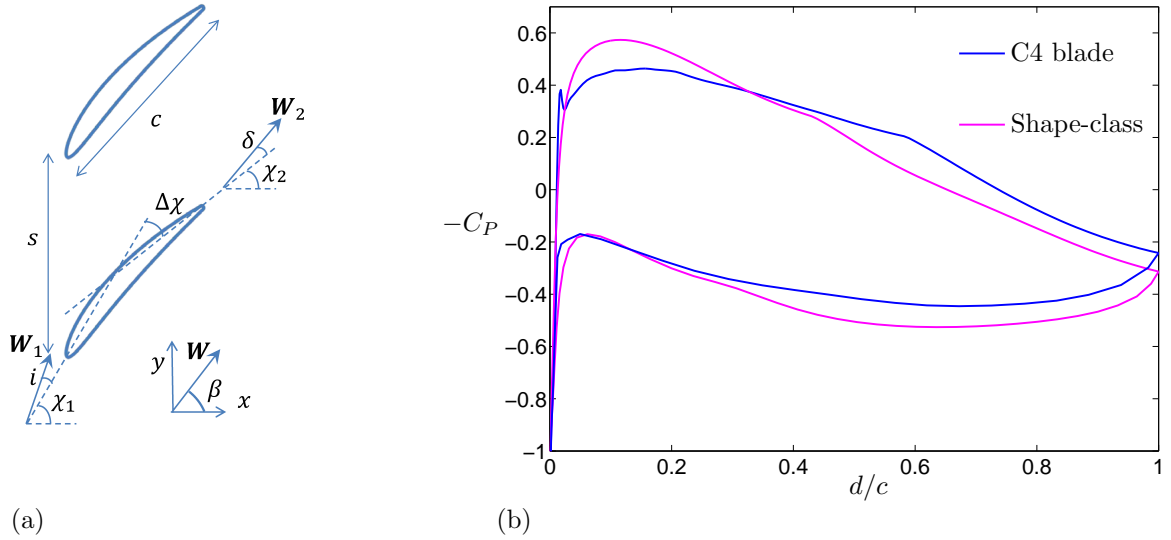


Figure 2. (a) Cascade geometry with definitions of angles and key dimensions. (b) C_P distribution around a C4 blade and shape-class blade (details of run in Table 1).

Table 1. Comparison of blade parameters for two sections of maximum thickness $t_{\max} = 0.08c$ at $Re = 50,000$, $M = 0.1$ at design incidence. The first six entries are design inputs, while the last three entries are typical outputs.

Blade	d_{\max}/c	χ_1	χ_2	ϕ^*	ψ^*	s/c	Y_P	δ	η
C4 blade	0.3	65°	40°	0.53	0.34	1.1	0.038	11.7°	92.4%
Shape-class blade	0.2	65°	40°	0.53	0.34	1.1	0.034	10.1°	94.0%

III. Low- Re design study

III.A. Effect of inlet angle

To begin with, we consider a simple C4 thickness distribution¹¹ which we lay on to a circular camber line with different inlet and exit angles. The leading edge is a circular section with tangency enforced at the joining points with the main thickness distribution. The maximum thickness is scaled to be $t_{\max}/c = 0.08$. The inlet angles are chosen so that the design flow coefficient lies in the range $\phi^* = [0.3 \ 0.6]$; this range corresponds to the lower end of the typical range for large-scale compressors.¹² The blade exit angle χ_2 is set using a fixed design stage loading coefficient ψ^* . At every design flow coefficient a MISES sweep of runs is performed in which the incidence angle is continuously varied from negative incidence to positive incidence so that we have a good picture of the performance of the blade section also at off-design conditions. The pitch-to-chord ratio for every design flow coefficient (and so for every set of blade angles χ_1 and χ_2) is found by setting the Lieblein diffusion factor to $D_F = 0.425$ at design.

Results in terms of loss coefficient and deviation angle are presented in Figure 3. The loss coefficient is significantly reduced across the whole range of incidence angles for increasing flow coefficient; this is interpreted as being the result of a larger amount of flow guidance at low blade angles, i.e. the streamwise

extent of duct-like flow between the throat and the exit is increased. This acts to reduce the loading on the blade section, reducing the adverse pressure gradients on the suction surface and the susceptibility to flow separation. The dramatic differences between the losses on these blade profiles at positive incidence is to be attributed to large separations on the low- ϕ^* profiles, which are increased at our $Re = 5 \times 10^4$. On the other hand and perhaps counter-intuitively, the deviation angle goes up as we increase the flow coefficient; this could be because the constant D_F condition means the pitch-to-chord ratio is actually significantly smaller for low ϕ^* leading to lower deviations. In any event, the increase in deviation is at most of 2° with absolute deviation values being typically $> 10^\circ$ so this result is not as significant as the substantial change in loss coefficient. This will be clearer when we consider results in terms of rotor efficiency. A final consideration that was found to be consistent among almost all blade sections that were studied, is that the minimum loss coefficient occurs at negative incidence. Our choice of a negative design incidence reflects this trend, which underlines the important role that the suction surface, and its associated separation regions, play in determining the blade performance.

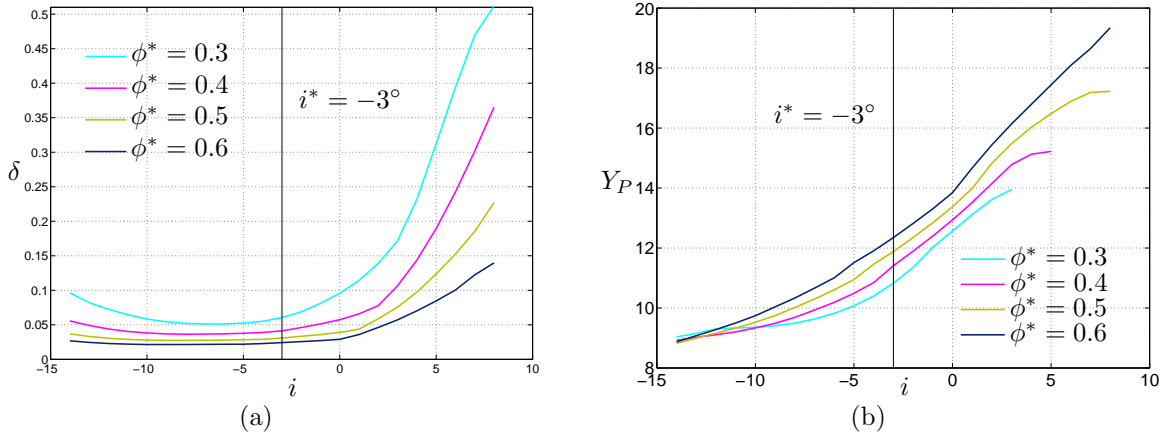


Figure 3. (a) Loss coefficient and (b) deviation angle as a function of the incidence angle for different design flow coefficients. The vertical black lines denote the design incidence at which ϕ^* and ψ^* are computed.

III.B. Effect of turning

We now consider various values of design stage loading coefficient in the range $[0.25 \ 0.45]$, which, in view of the greater challenge of turning a flow at low Re without incurring in large separations, is on the lower side of values used in typical compressors.¹² We keep the design flow coefficient constant at $\phi^* = 0.5$. Again, the pitch-to-chord ratio is set based on a design diffusion factor of 0.425, except for case $\psi^* = 0.45$ where this would have lead to a very small pitch-to-chord ratio $s/c \approx 0.2$, and in this case we use $D_F = 0.45$. Results from MISES runs are given in Figure 4. For lower turning imparted on the flow the losses are lower for most incidences as expected, while the deviation angle is decreased at low incidences for small ψ^* but increased at high positive incidence due to the effect of the greater pitch-to-chord ratio. From these first considerations of flow and loading coefficients it would appear that high flow coefficients with relatively low loading coefficients will favour the highest efficiency. However we will defer further discussion on optimal bounds for ϕ^* and ψ^* to the next section, when we vary both coefficients together.

III.C. Variation of inlet angle and turning

We now investigate the combined effect of varying blade inlet angle and blade turning. We consider ranges of $\chi_1 = [52^\circ \ 76^\circ]$ and $\Delta\chi = [14^\circ \ 36^\circ]$ at intervals of 3° for both angles and perform MISES runs at every point of the two-dimensional matrix. These angles correspond to a range of design flow coefficient $\phi^* = [0.32 \ 0.87]$ and design loading coefficient $\psi^* = [0 \ 0.61]$. The pitch-to-chord ratio at every point is again found by setting $D_F = 0.425$, but lower and upper bounds are placed at pitch-to-chord values $s/c = 0.4$ and $s/c = 2$. The results are presented in terms of rotor efficiency, where the numerical cascade is taken to be the rotor in the relative frame, and the axial flow constancy is no longer employed since direct

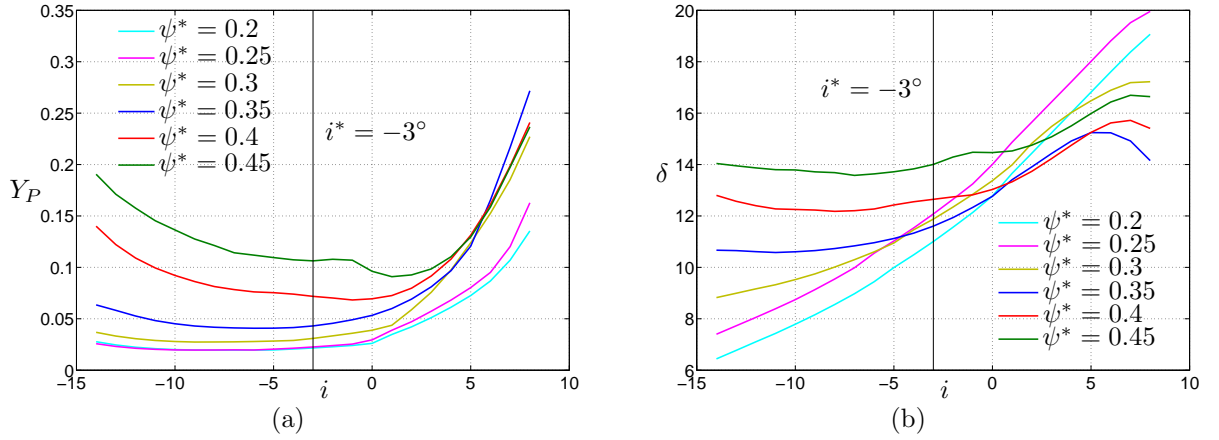


Figure 4. (a) Loss coefficient and (b) deviation angle as a function of the incidence angle for different design stage loading coefficients.

flow field computations are available. This is also true for the stage loading coefficient ψ^* , which is now calculated correctly. In Figure 5 a colour map of rotor efficiency is given as a function of flow and loading coefficients. From this plot there is a large high efficiency region ranging from the lowest loading coefficient $\psi^* \approx 0.15$ to a value of ψ^* that is dependent of the particular flow coefficient that we are considering. The white area in the top left corner has high loading coefficients with low flow coefficients, which results in large separations on the blade suction surface. At these high loadings, even with very low pitch-to-chord ratio to keep $D_F = \text{const}$, the deceleration of the flow leads to separation. This therefore corresponds to a region with very low efficiency and the boundary between the colour map and the white area can be considered as the boundary of acceptable designs. For example, for $\phi^* = 0.5$ the maximum acceptable value of loading is $\psi^* \approx 0.35$ before a severe reduction in efficiency occurs. This can also be seen in Figure 4(a) where there is a jump in the loss coefficient between $\psi^* = 0.35$ and $\psi^* = 0.4$. These results are dependent on the value of D_F chosen as well as on the bounds set upon s/c , which are responsible for some of the high gradients in η in Figure 5. They are also specific to the C4 blade profile family and it is therefore of interest to consider alternative thickness distributions, which we will do in the following section.

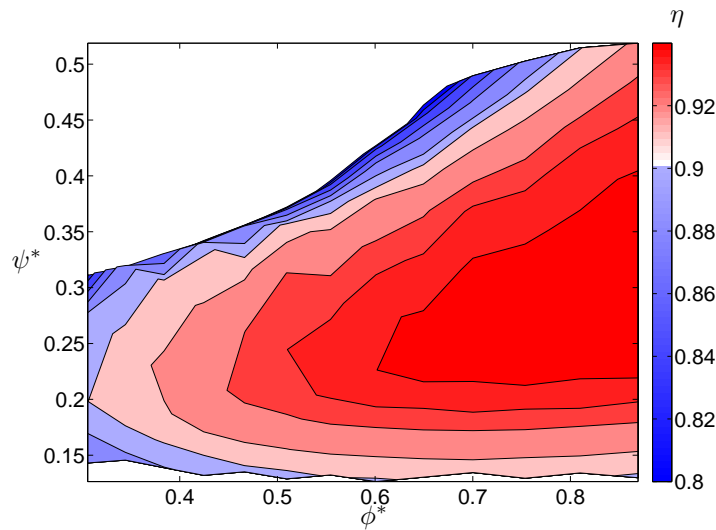


Figure 5. Rotor efficiency η at design incidence $i = -3^\circ$ as a function of flow coefficient and stage loading coefficient.

III.D. Modifying the thickness distribution

III.D.1. Shape/class function approach

There are a number of ways to specify the thickness distribution and final shape of an airfoil or a blade section, including polynomial curves, B-splines or simply a discrete set of coordinate points as in the case of the C4 profile used before. We choose to use a method specifically designed to define airfoil shapes, the shape/class function approach.¹³ This method uses a class function, which in its simplest form describes an airfoil with a parabolic leading edge that blends towards a linearly tapered trailing edge. The class function $C(x)$ is then multiplied by a shape function $S(x)$ that defines the thickness distribution between the two airfoil edges. More specifically the thickness distribution $z(x)$ is defined as

$$z(x) = S(x) \underbrace{\sqrt{x(1-x)}}_{=C(x)} + z_{te}x \quad (5)$$

where $C(x)$ is defined and a finite trailing edge thickness z_{te} is allowed for. In this equation z can be considered as the half-thickness from the camber-line of a symmetric airfoil and x is the distance along the camber line which is of unit length, i.e. chord $c = 1$. The shape function is of course arbitrary and could again be defined using splines or other methods. We choose a simple approach and use shape functions of the following family, $S(x) = A \cos(kx) + Bx + C$ where A, B, C and k are modifiable constants. The first constant A is chosen to be small and positive (typically $A = 0.01$) giving a front biased blade thickness, considering also that k is chosen either as $k = 1$ or $k = 1/2$. The values of B and C are then found by specifying an x location at which the thickness distribution is to peak, i.e. the maximum thickness point, as well as the value of this maximum thickness. For example, two thickness distributions calculated using this method are given in Figure 6 together with their corresponding shape functions. The final step to create the blade shape is to lay this symmetric thickness distribution onto a camber line, and, again, for simplicity, a circular camber line with its constant curvature is our preferred choice.

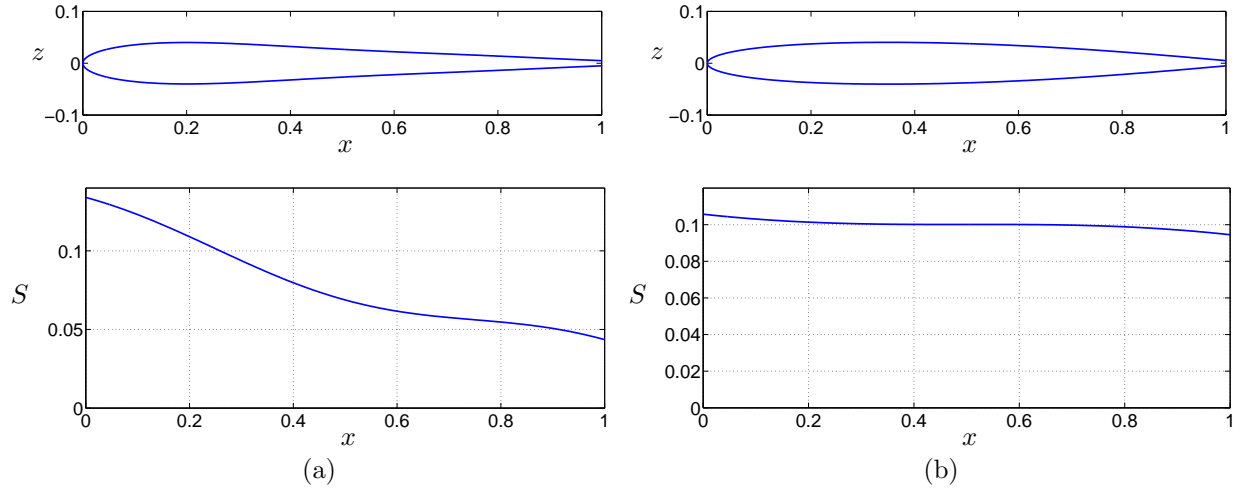


Figure 6. Thickness distribution and shape function for airfoil with maximum thickness (a) at $x = 0.2$ (b) at $x = 0.4$. Maximum thickness $t_{\max} = 0.08$ in both cases.

III.D.2. Effect of changing the maximum thickness location

Having established a method to create thickness distributions peaking at a chosen location, we generated a number of designs with maximum thickness in the range $x = [0.2 \ 0.5]$. We lay these thickness distributions on a circular camber line with inlet angle $\chi_1 = 55^\circ$ and exit angle $\chi_2 = 27^\circ$, giving a flow coefficient $\phi^* = 0.78$ and a stage loading coefficient $\psi^* = 0.39$. According to Figure 5 these values of ϕ^* and ψ^* already correspond to a region of high efficiency for a generic C4 blade, and we wish to explore another dimension of the design space to see if further performance gains are possible.

In Figure 7 we present MISES sweeps for the various blades with maximum thickness at different locations along the camber line d_{\max}/c . The loss coefficient plot shows that for incidences below $i = 6^\circ$ the losses are

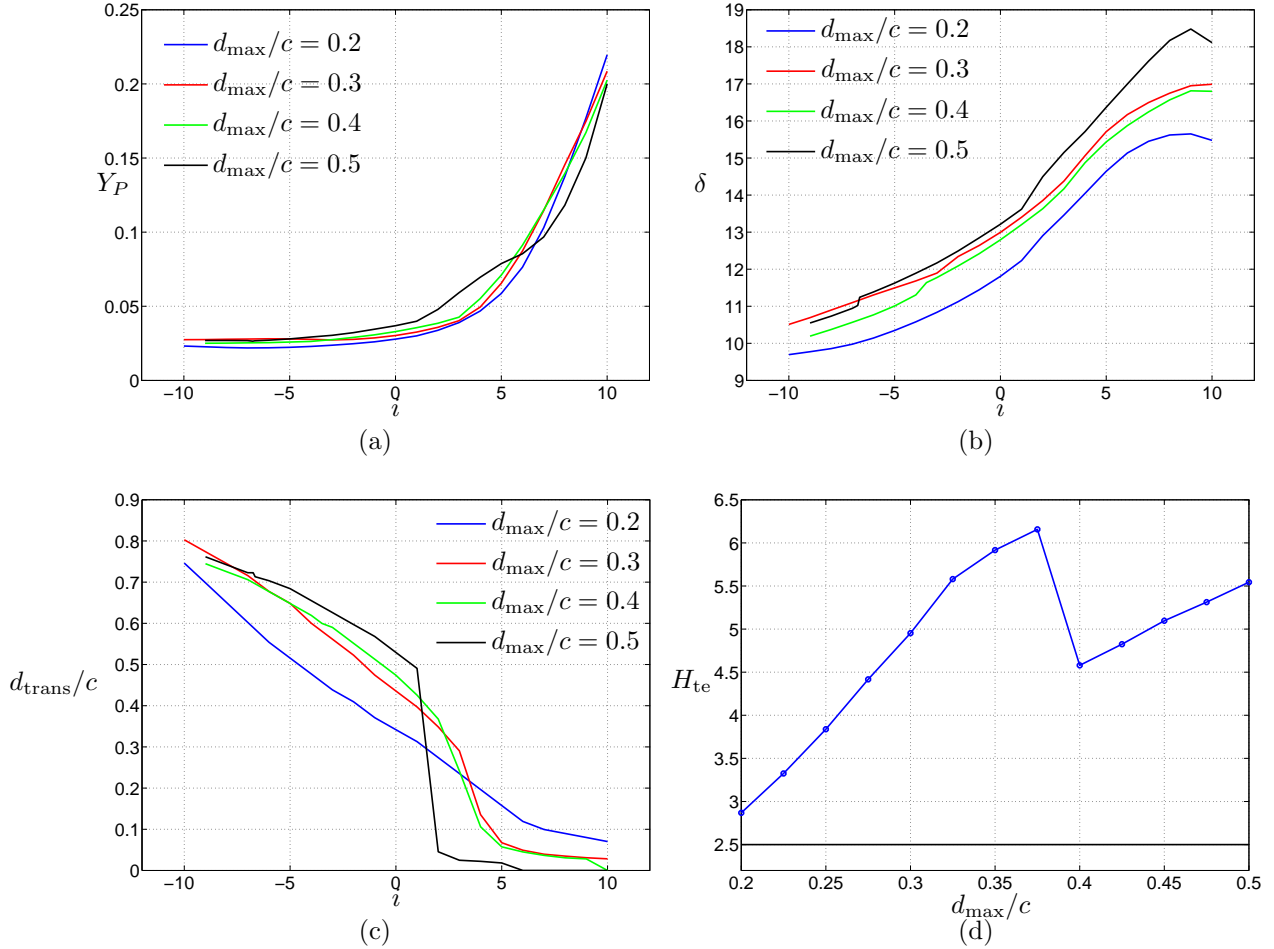


Figure 7. Sweep of MISES runs for blade profile peaking at different locations d_{max} . Results in terms of (a) loss coefficient, (b) deviation angle and (c) transition location on suction side. In (d) the boundary layer shape factor at the trailing edge at design incidence $i = -3^\circ$ is given as a function of maximum thickness location. The solid black line is at $H = 2.5$ which is the shape factor above which a turbulent boundary layer is considered to have separated.

lower for blades with maximum thickness towards the front, whereas the picture changes at more positive incidence when the blades that have maximum thickness further downstream have lower loss. The plot of deviation against incidence, however, shows that at all inlet angles there is reduction in deviation for the front-thickened blades. To understand these variations in performance, it is interesting to inspect the transition location on such blades, given in Figure 7(c). Now, it can be observed that at negative incidence the more the maximum thickness is brought to the front the earlier the transition to turbulence. This is because front-thickened blades have a greater adverse pressure gradient at the front of the blade that encourages early transition as can be seen in Figure 2(b) comparing the C_P distribution of a C4 blade and a front-thickened blade. After transition, the front-thickened blade has a gentler diffusion that delays turbulent separation, a major contributor to the loss. The result of this is an overall better performance at negative incidence (and even up to $i \approx 6^\circ$) of a front-thickened blade. The higher value of C_P at exit for the front-thickened blade shows that for the same blade turning we achieve higher pressure rise. It is this comparative reduction in loss and increase in flow turning that is important for our design investigation, more than the actual values of deviation and loss. This is because the absolute values are highly dependent on the flow solver and may be very different from the full operative losses of compact compressors (where we have also 3D losses).

The fact that front-thickened blades present less separations at design can be seen from Figure 7(d) where the boundary layer shape factor at the trailing edge H_{te} is plotted against the maximum thickness location. All blade thickness distributions present $H_{\text{te}} > 2.5$ and so are separated at the trailing edge,¹⁴ but the greater d_{max} the greater H_{te} highlighting larger and larger separation regions. Hence by choosing a design

with maximum thickness towards the front of the blade we minimize the turbulent separation towards the back of the blade. The case with thickness distribution peaking at $d_{\max}/c = 0.2$ has $H_{te} = 2.8$ and separation occurring towards the back of the blade. By inspection of the H -distribution on this blade (not shown), turbulent separation occurs at 95% chord. This is therefore our choice as an optimum thickness distribution.

III.D.3. Effect of ϕ and ψ on front-thickened blade

We now proceed to inspecting the performance variation of our best thickness distribution for low- Re , a front-thickened blade ($d_{\max}/c = 0.2$), at variation of blade metal angles. To this end a number of MISES runs at design conditions and with different camber lines were performed. Results in terms of efficiency are presented in Figure 8, where also a colour map showing the transition location throughout the two-dimensional design space is given. The good correlation between Figures 8(a) and (b) confirms our previous supposition that early transition is associated with lower losses and higher efficiencies. This was already suggested by the work of Roberts³ who used trip wires on low- Re blades to incite transition and found loss reductions.

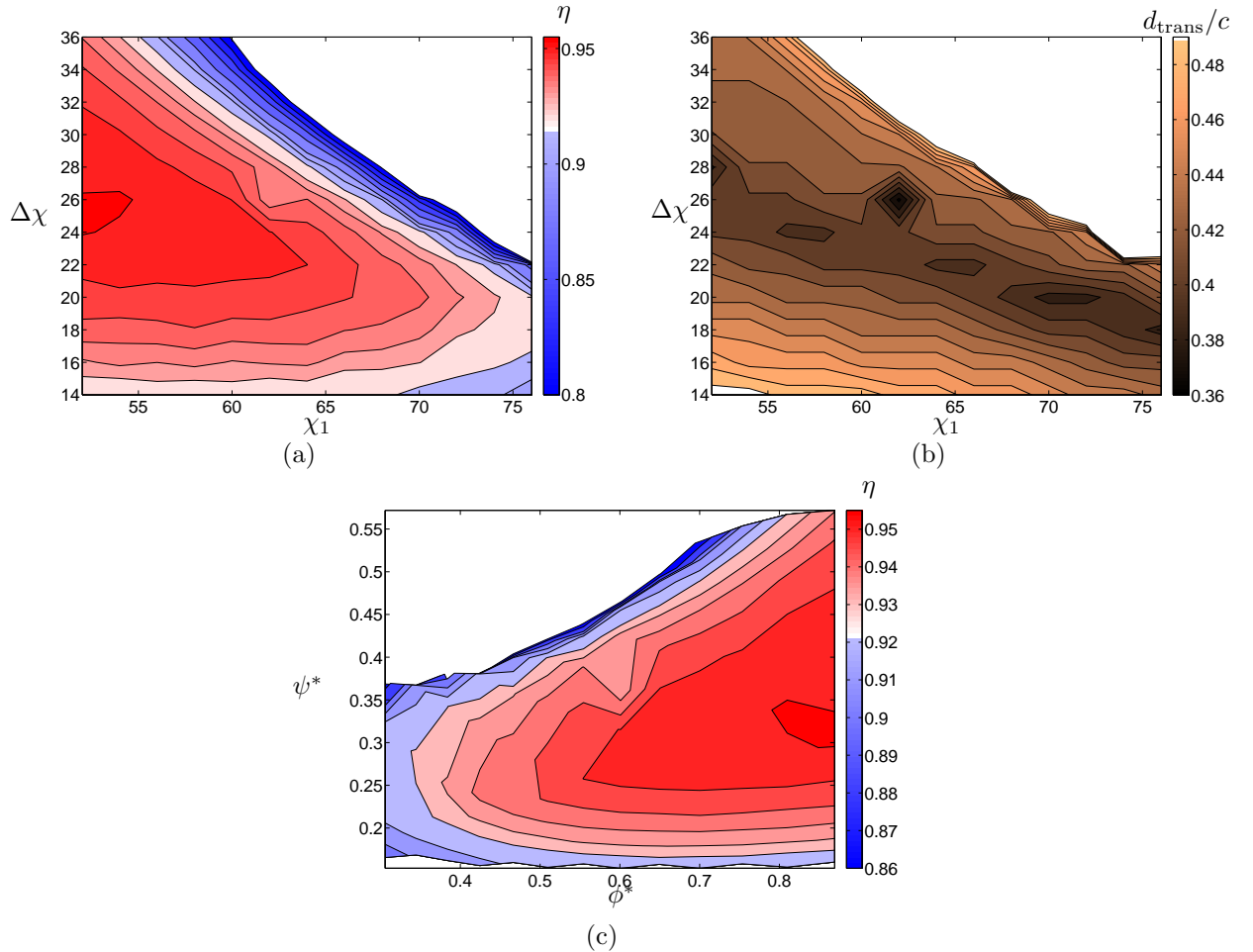


Figure 8. Variation of performance for front-thickened blade at design incidence: (a) rotor efficiency and (b) transition location as a function of inlet angle χ_1 and camber $\Delta\chi$. (c) Colour map of efficiency on transformed space in terms of flow and loading coefficients.

The plot in Figure 8(c) can be used to identify new bounds on flow and loading coefficients. The picture is similar to Figure 5 with high flow coefficients allowing greater and greater amounts of loading. But the exact values of allowable ψ^* at a given ϕ^* have increased for this front-thickened blade as have the overall values of efficiency (by about 2% in the high efficiency regions). For example at $\phi^* = 0.5$ values of ψ^* up to 0.4 are acceptable, which is greater than the 0.35 value for the family of C4 blades. So overall by setting the maximum thickness towards the front, we have identified a design modification that is beneficial

at low- Re . This is especially true at negative up to mild positive incidence and so will especially be useful for application that do not require an extensive positive incidence range. For example, in the optimised design with $d_{\max}/c = 0.2$ the positive incidence range is up to $i = 6^\circ$ in order to keep the 2D loss below a reasonable figure of 7% (see Figure 7); this corresponds to a positive incidence range of 9° from $i = -3^\circ$ at design, or a 29% reduction in mass flow, which may not be enough for all applications (e.g. vacuum cleaners need a very extensive operating mass flow range).

III.E. Choice of pitch-to-chord ratio

In this final part of the design study we explore the effect of the pitch-to-chord ratio. Thus far, s/c was selected by using a diffusion factor at design together with an assumed value of deviation. This is the typical practice in modern compressor design.¹² However, the picture may change at low Reynolds numbers, where suction side diffusion is responsible for boundary layer separation and could be a limiting factor. To investigate this, we varied pitch-to-chord ratio for a C4 blade and the optimised front-thickened blade. We then ran MISES sweeps for all s/c values and the results are presented in Figure 9. The loss coefficient and deviation are at $i = 0^\circ$ (different than the previous design incidence to allow a comparison with cascade experiments with data points every 5°), while the incidence range $\Delta\beta^+$ is the positive incidence range from this incidence up to an incidence where the loss coefficient is double the value at $i = 0^\circ$. We have added to Figure 9 the results from cascade experiments, which will be discussed further in the next section. The geometry for the experimental runs is the front-thickened blade with different pitch-to-chord ratios. In all cases the inlet blade angle is $\chi_1 = 55^\circ$ and blade camber is $\Delta\chi = 28^\circ$, which are values corresponding to a high rotor efficiency (see Figures 5 and 8). The front-thickened blade with these angles is denoted Shapespace28.

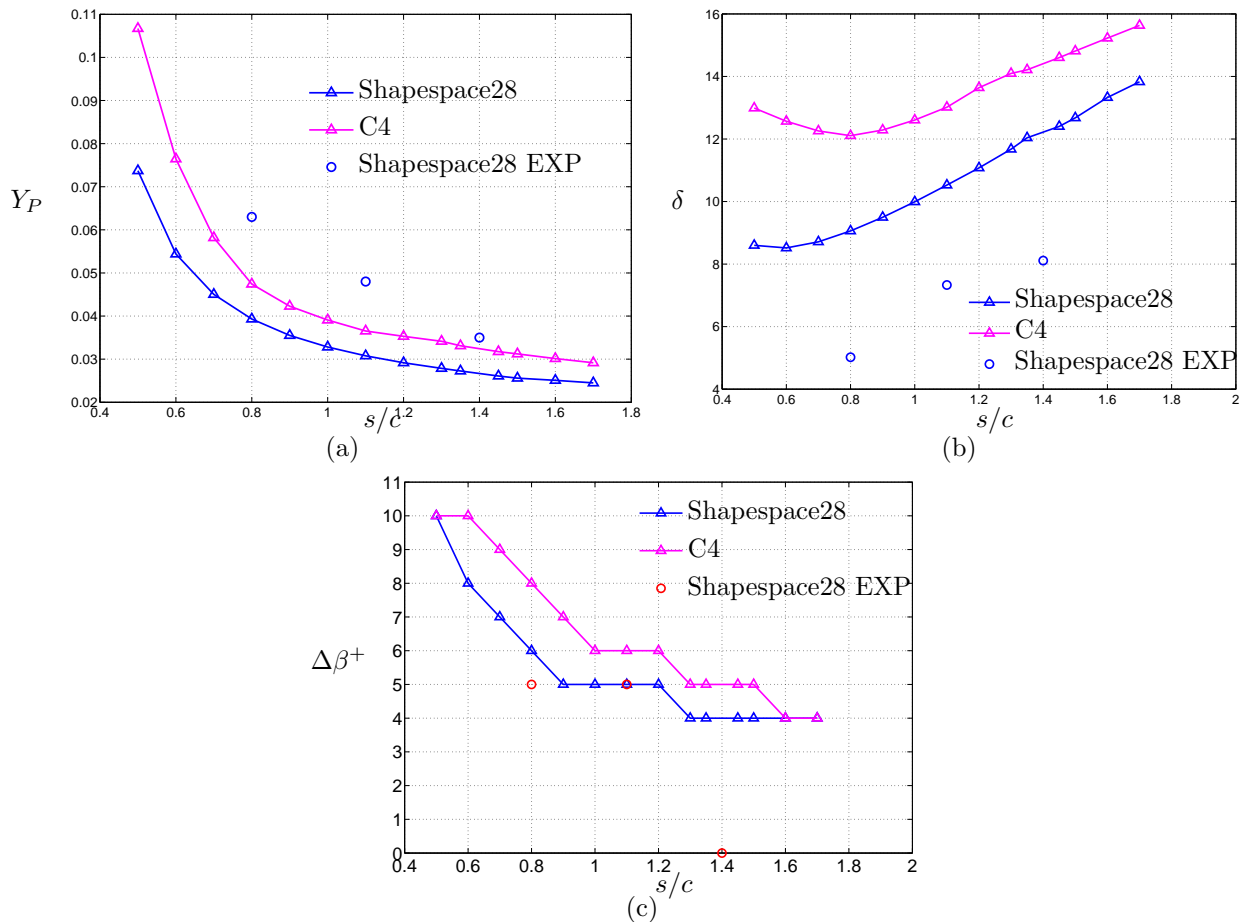


Figure 9. Effect of pitch-to-chord variation on blade performance: (a) loss coefficient, (b) deviation angle and (c) positive incidence range.

By inspection of Figure 9(a) it is clear that the losses steadily decrease for a given blade shape if we increase the pitch-to-chord ratio. This is because at design incidence the separation regions are limited and skin-friction losses and separation losses are of the same order. To decrease the pitch-to-chord ratio is to increase the total wetted area, which is directly proportional to the skin-friction losses for a constant value of skin friction coefficient C_f . Hence as we increase s/c separation losses stay about the same but skin-friction losses increase and the overall loss figure goes down. On the other hand, as is evident from Figure 9(b), the deviation angle goes up with increasing s/c , as the flow is less guided, resulting in an overall reduction in flow turning. In terms of peak efficiency however the effect of the loss reduction is greater than the effect of the increase in deviation, so that the highest design efficiency is found at the greatest pitch-to-chord ratios. In the case of the Shapespace28 blade, $\eta_{\max} = 95.5\%$ at $s/c = 1.5$, corresponding to a diffusion factor $D_F = 0.51$. Therefore for single-operating-point performance values of diffusion factor as high as $D_F = 0.5$ are allowed.

The picture changes if we turn to Figure 9(c), which shows the positive incidence range $\Delta\beta^+$ measuring the value of positive incidence at which the loss coefficient is double its value at zero incidence. This gives an idea of the 2D stall margin of such a compressor section. Now, $\Delta\beta^+$ drops rapidly with s/c up to low values of $\Delta\beta^+ = 4^\circ$. If a minimum requirement is to have a positive incidence range of at least $\Delta\beta^+ = 6^\circ$ (or a mass flow range $\Delta\dot{m}/\dot{m} > 21\%$ for this flow coefficient) then the maximum allowable s/c would be $s/c = 0.8$ for Shapespace28, at which value we have $D_F = 0.45$. This is the typical value chosen for large-scale compressors, which is a conservative figure that turns out to be appropriate even at the more demanding low- Re conditions.

The experimental values for loss coefficient and deviation are significantly offset compared to the MISES results. However the trends with varying pitch-to-chord ratios are all maintained between computational and experimental runs. The optimum pitch-to-chord ratio from the experiments could be either $s/c = 0.8$ or $s/c = 1.1$, both of which have high design efficiencies $\eta > 91.5\%$ at zero incidence and $\Delta\beta^+ \approx 5^\circ$ (the low incidence resolution in the experimental results does not allow this value to be pinned down more accurately).

IV. Cascade Experiments

To complement our design study in MISES, experiments were performed in an open wind tunnel at the Whittle Laboratory. The experimental rig is shown in Figure 10; it is modular allowing different 3D printed cascades to be tested. Five blade sections were tested as listed in Table 2. Quantitative results were obtained by traversing a three-hole probe downstream of the cascade, thereby measuring profiles of stagnation pressure and flow angle in the wakes. Hence it was possible to compute loss coefficients and deviation angles at incidence intervals of 5° . A summary of the results at zero incidence are presented in Table 2. While the absolute values are in discrepancy with the MISES results, the trends for all three performance indicators are matched. In particular, for the same blade inlet angle and camber, a shape-class thickness distribution peaking at $d_{\max}/c = 0.2$ (our optimised thickness distribution) performs significantly better than a corresponding C4 baseline blade, with lower loss and deviation and a 4% efficiency increase. Also the pitch-to-chord behaviour is well represented, with higher s/c giving high peak efficiency but a growing deviation (see also Figure 9). In conclusion the design choices for low- Re compressor sections outlined in the previous section are confirmed by the cascade tests.

Flow visualisation using fluorescent paint was also performed allowing the identification of separation and reattachment points on the blade suction surfaces. The salient points on the Shapespace28sc1.1 blade across the entire incidence range are given in Figure 11. Flow visualization images from which these points are obtained are presented at three incidences, $i = -5^\circ$, 0° and 5° to highlight the different flow structures. At the negative incidence there is a laminar separation bubble of significant size towards the aft of the blade, the reattachment point being at 85% chord. At zero incidence the LSB moves towards the front of the blade and is reduced in size, but there is a further turbulent separation at 90% chord, impacting the loss substantially. Finally at the positive incidence the boundary layer separates at the leading edge and then reattaches turbulent shortly thereafter, and there is a large turbulent separation on the last quarter of the suction surface (note that at $i = 10^\circ$ there is open separation from the leading edge).

In Figure 11 the MISES transition points have been added as well the turbulent separation point, defined as the first point on the suction surface where we have turbulent flow with $H > 2.5$. The transition points at all incidences lie in between the laminar separation and turbulent reattachment points from the cascade tests, an encouraging result. However, it has to be pointed out that transition in MISES occurs invariably a

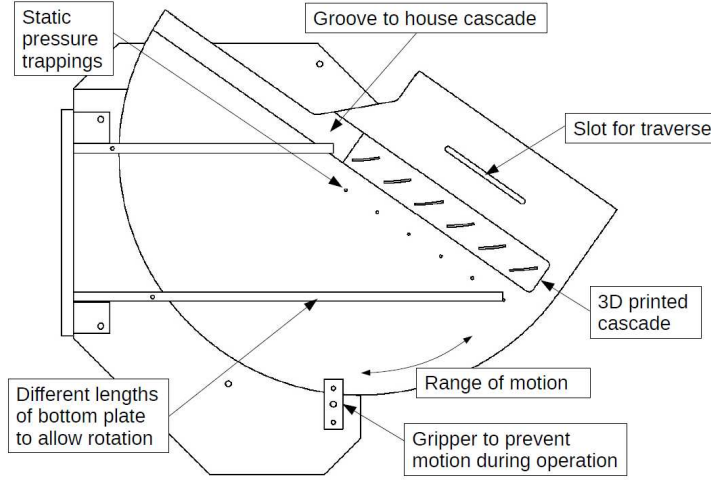


Figure 10. Experimental rig, showing rotating setup to allow changes in incidences as well as the inclined groove in which 3D printed cascades were inserted.

single grid point after the flow separates, when the skin friction coefficient C_f going negative, and this forces C_f back to positive values within another grid point. In this sense MISES successfully predicts the presence of a LSB, but these are always very short. In reality, as highlighted by the experiments, the LSBs at this Reynolds number are medium to long. This could be the reason for the systematic under-prediction of the loss in MISES. The turbulent separation points from MISES are in better agreement with the experiments, highlighting that the main challenge for CFD remains to capture accurately the LSB and its associated loss penalty.

Table 2. Blade profiles tested in cascade experiments at $Re = 4.9 \times 10^4$. Values of flow and loading coefficient given at zero incidence as well as loss, deviation and efficiency.

Blade	d_{\max}/c	χ_1	χ_2	$\Delta\chi$	ϕ^*	ψ^*	s/c	Y_P	δ	η
C4 baseline	0.3	55°	35°	20°	0.7	0.28	1.4	0.043	8°	90.8%
Shapespace20	0.2	55°	35°	20°	0.7	0.28	1.4	0.028	5.6°	94.8%
Shapespace28sc0.8	0.2	55°	27°	28°	0.7	0.45	0.8	0.063	5°	91.6%
Shapespace28sc1.1	0.2	55°	27°	28°	0.7	0.45	1.1	0.048	7.3°	93%
Shapespace28sc1.4	0.2	55°	27°	28°	0.7	0.45	1.4	0.035	8.1°	94.8%

V. Conclusions

A design study using MISES has been presented for compressor rotor sections at a representative low Reynolds number of $Re = 5 \times 10^4$. This Reynolds number is suitable for domestic appliance compressors. Flow coefficients as high as $\phi = 0.8$ are desirable for high rotor efficiency, while the allowable stage loading coefficients are dependent on the flow coefficient and at most reach $\psi = 0.5$. Highly loaded compressors with $\psi \approx 0.65$, which are a serious contender for high- Re design,¹⁵ are ruled out at low Re .

In terms of thickness distribution, a front-thickened blade was found to perform best in terms of all three performance indicators (loss coefficient, deviation angle and rotor efficiency) at design. The added thickness towards the blade front increases the loading over this portion of the blade and encourages early transition. The corresponding reduced aft loading means the turbulent flow does not separate until the very back of the blade which reduces loss and deviation. Such blades could be an ideal candidate for single-operating-point devices, as are blades with high pitch-to-chord ratio. However, when positive incidence range is as important as design efficiency, as in vacuum cleaners, the pitch-to-chord ratio has to be limited to maintain off-design performance. A value of Lieblein diffusion factor of $D_F = 0.45$ is found to be appropriate for a good design with about 20–25% mass flow range. Upward or downward modifications of D_F at design can be chosen to modify the trade between peak efficiency and range. Cascade experiments confirm the improvements in

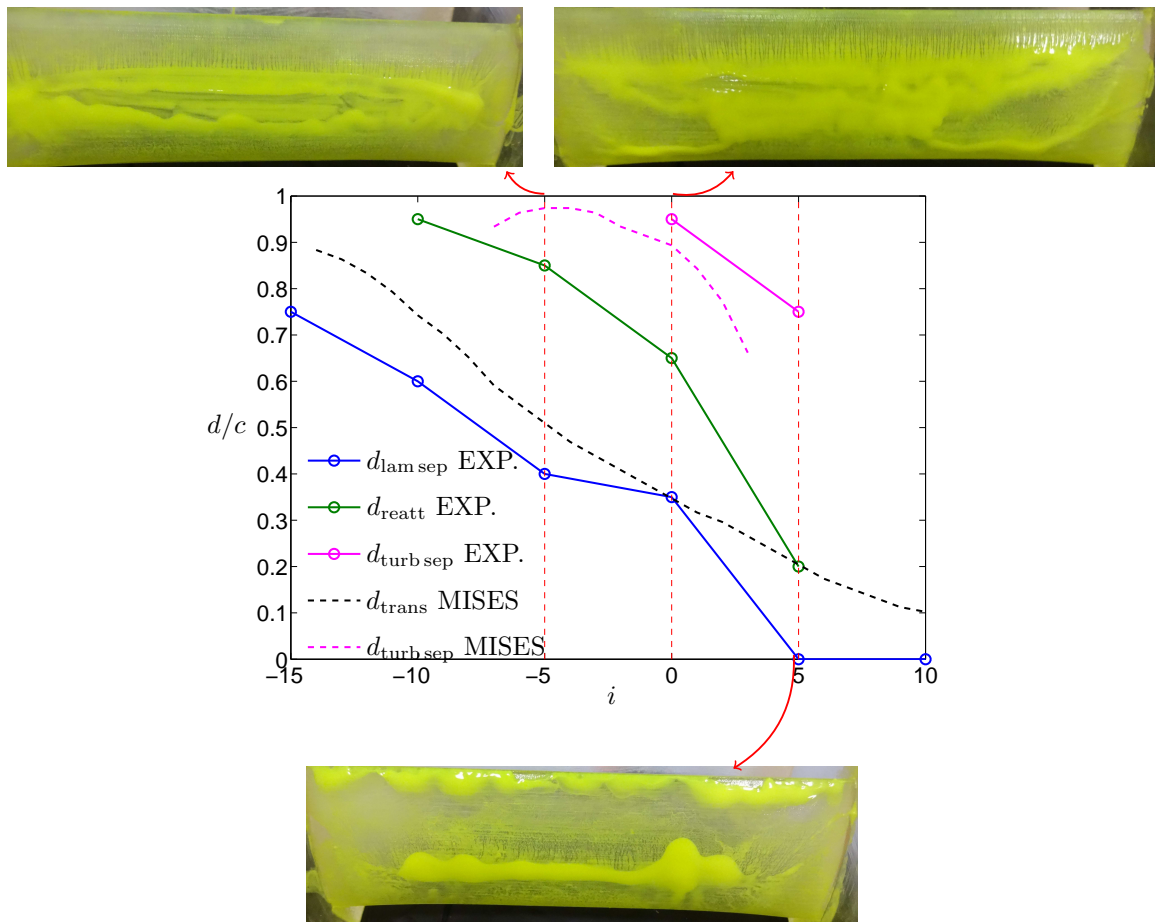


Figure 11. Separation and re-attachment points from flow visualization compared against MISES transition points and turbulent separation points as a function of incidence angle. Flow visualization photos are shown at three representative incidences. The leading edge of the blade is at the top of the images.

moving from a C4 blade to a front-thickened shape-class blade as well as the trends in terms of pitch-to-chord ratio. Flow visualization has highlighted the separation and reattachment points, showing the presence of long laminar separation bubbles that are not accurately depicted in MISES.

Finally, recommendations for future work include using high-fidelity CFD to better capture the transition process and the associated laminar separation bubble. At Reynolds numbers of 50,000 it is possible with current computer capabilities to perform Large Eddy Simulations (LES) and even Direct Numerical Simulations (DNS), which resolve all scales of turbulent motion. This is not only important to obtain accurate quantitative predictions of performance, but also to gain a better understanding of the the distinct flow features of low Reynolds number compressors, which could inform future design choices in this area.

Acknowledgments

We would like to thank John Saunders for his help in building the cascade rig and Rob Miller, Mark Johnson and Konstantinos Pantelidis for their valuable input during the course of the project. Financial support from Dyson Appliances is gratefully acknowledged.

References

- ¹Choi, M., Baek, J.H., Chung, H.T., Oh, S.H. and Ko, H.Y., *Effects of the low Reynolds number on the loss characteristic in an axial compressor*, Proceedings of the Institution of Mechanical Engineers, Vol. 222, Part A: Journal of Power and Energy, 2008.
- ²Shyy, W., Lian, Y., Tang, J., Viieru, D. and Liu, H., *Aerodynamics of low Reynolds number flyers*, Cambridge University Press, 2006.
- ³Roberts, W.B., *Axial compressor blade optimization in the low Reynolds number regime*, AIAA Journal, Vol. 17, No. 12, December 1979.
- ⁴Coull, J.D. and Hodson, H.P., *Unsteady boundary-layer transition in low-pressure turbines*, Journal of Fluid Mechanics, Vol. 681, pp.370-410, August 2011.
- ⁵Rao, V.N., Jefferson-Loveday, R., Tucker, P.G. and Lardeau, S., *Large eddy simulations in turbines: influence of roughness and free-stream turbulence*, Flow, Turbulence and Combustion, Vol. 92, Issue 1-2, pp.543-561, January 2014.
- ⁶Drela, M. and Youngren, H., *A users guide to MISES 2.63*, MIT Aerospace Computational Design Lab, February 2008.
- ⁷Lian, Y. and Shyy, W., *Laminar-turbulent transition of a low Reynolds number rigid or flexible airfoil*, AIAA Journal, Vol. 45, No. 7, July 2007.
- ⁸Drela, M. and Giles, M.B., *Viscous-inviscid analysis of transonic and low Reynolds number airfoils*, AIAA Journal, Vol. 25, No. 10, October 1987.
- ⁹Lieblein, S., Schwenk, F.C. and Broderick, R.L., *Diffusion factor for estimating losses and limiting blade loadings in axial-flow-compressor blade elements*, NACA RM E53D01, 1953
- ¹⁰Hodson, H.P., *Blade to blade flowfields in axial flow turbomachines*, Cambridge Turbomachinery Course, Volume 1, pp. 35–75, 2012.
- ¹¹Cumpsty, N.A., *Compressor aerodynamics*, Appendix: Blade profile families for axial compressors, John Wiley, 1989.
- ¹²Denton, J.D., *Introductory review of basic principles*, Cambridge Turbomachinery Course, Volume 1, pp. 1–31, 2012.
- ¹³Kulfan, B.M. and Bussolletti, J.E., *“Fundamental” parametric geometry representations for aircraft component shapes*, 11th AIAA Multidisciplinary Analysis and Optimization Conference, 6–8 September 2006.
- ¹⁴Schlichting, H., *Boundary layer theory*, Springer, 2000.
- ¹⁵Dickens, T. and Day, I., *The design of highly loaded axial compressors*, Journal of Turbomachinery, Vol. 133, July 2011.